KuROS: A new airborne Ku-band Doppler radar for observation of the ocean surface

Danièle Hauser, Gérard Caudal, Christophe Le Gac, René Valentin, Laurent Lapauw, Lauriane Delaye, Nicolas Pauwels, Céline Tison

KuROS : A new airborne Ku-band Doppler radar for observation of the ocean surface

D. Hauser, G. Caudal, C. Le Gac, R. Valentin,
L. Lapauw, L. Delaye, N. Pauwels
Université Versailles St-Quentin
Sorbonne Universités, UPMC Univ. Paris 06 CNRS/ INSU, LATMOS-IPSL
11 Boulevard d'Alembert F-78280 Guyancourt, France
daniele.hauser@latmos.ipsl.fr

C. Tison
CNES
18 Avenue Edouard Belin F-31420 Toulouse, Cedex9, France
celine.tison@cnes.fr

***Abstract*— We present the new airborne Ku-band Doppler radar KuROS, designed for wind/wave observations of the ocean surface. First results obtained from observations collected during two field campaigns held in 2013 are also illustrated. Both intensity and Doppler information have been used to estimate the direction wave spectra of ocean waves. Results on radar cross-section and directional spectra of ocean wave are assessed trough comparison with independent information. We also present a preliminary analysis of the speckle energy density spectrum as a function of sea state conditions.**

Keywords—airborne radar; ocean surface; surface wind; ocean surface waves. Speckle

I. INTRODUCTION

In the context of the preparation of the future CFOSAT (China-France Oceanography satellite) satellite mission [1], we have developed a new airborne radar, called KuROS (Ku-band Radar for Observation of Surfaces). Indeed CFOSAT will carry two instruments: SWIM (designed and manufactured by France), which is a Ku-Band wave scatterometer (incidence angles between 0 to 10°) aimed at measuring the ocean directional wave spectra, and SCAT (designed and manufactured by China), which is a Ku-Band wind scatterometer (incidence angles around 40° with a wide swath) which will provide the surface wind vector. The primary aim of KuROS is to optimize the choices made for the implementation of the CFOSAT satellite, and to serve as a tool for the geophysical validation of the CFOSAT surface wind and wave measurements once launched. So, the KuROS specifications have been chosen to cover the geometry of both SWIM and SCAT. Another important objective of the KuROS radar is to explore the characteristics of the kinematics of the sea surface. For this purpose, in addition to measuring the normalized radar cross section σ_0 KuROS has the ability to measure the Doppler velocity of the radar echo.

This paper presents the KuROS radar, methods and results on radar cross-section, directional ocean wave spectra and speckle estimates. More details can be found in [2].

II. GENERAL CHARACTERISTICS AND PERFORMANCES OF THE RADAR

KuROS is an airborne Ku-band (13.5 GHz) radar, which has been designed to cover a large range of incidence angles (0-50°) and azimuth angles (0-360°) in order to address the geometry of observations of the two payload instruments (SWIM and SCAT) of the CFOSAT satellite mission. In addition, a Doppler measurement capability has been designed for KuROS. Note that this capability is not implemented in SWIM and SCAT. The whole airborne system is mounted in an ATR42 aircraft, operated by the SAFIRE unit ("Service des Avions Français Instrumentés pour la Recherche en Environnement"), and the conditions of use of KuROS are specified to allow measurements from flights from about 500 m height to about 3000 m height above the surface.

In order to address the question of measuring both wind and waves, the KuROS antenna system is composed of two printed-array antennae: a HH-pol low incidence (called LI) antenna pointed to 14° incidence with respect to nadir and the dual-pol (HH/VV) medium incidence (called MI), antenna pointed to 40° incidence. The geometry of observation is illustrated in Fig. 1. The LI antenna aims at measuring wave spectrum as SWIM and the MI antenna aims at measuring wind vectors as SCAT.

The main characteristics of the radar are given in Table 1. Both antennae have a ±10° elevation and ±4° azimuth one-way beam-width. This relatively large aperture is required to estimate ocean wave spectra from a real-aperture radar at small-incidence (see [3], [4]). Both antennae have been tested in anechoic chambers to determine their lobe patterns. However, when integrated within the body of the aircraft, it turned out that the lobe of the MI antenna was not nominal. This is attributed to the presence of a metal collar used to adjust the antenna system within the body of the plane and this problem is presently under study. For this reason, the results presented here are focused on the observations performed with the LI antenna. The antenna system can be controlled either to rotate over 360° around the vertical axis at a variable rotation speed, or to stop at a fixed azimuth angle.

The transmitted wave is a pulsed chirp whose bandwidth is centered around 13.5 GHz. The transmitted bandwidth has been chosen in order to achieve a high range and horizontal resolution: 100 MHz for LI antenna and 30 MHz for the MI antenna, corresponding to a range resolution of 1.5 m (close to SWIM specifications) and 5 m, respectively. Because of the large range of distances to be sampled (flight altitudes from 500m to 3500m, incidences from 0 to 50°), and to some real-time constraints, several chronograms of transmitted pulses are used, depending on flight altitude and antenna (see Table 2). Typically for the LI antenna used from a 2000 m flight-level the pulse length and PRF are respectively 10.33 μs, and 35 kHz. All these modes are pre-loaded in the control unit and chosen by the operator during flights. At the reception, after going through the two switches and a circulator, the received chirps are sent to the low noise amplifier, and then filtered to limit the noise band and conserve only the upper band. The microwave signal is down converted with the same frequency source oscillator as used in the transmitter part. The signals are then amplified, filtered by an anti-aliasing filter and transmitted to the digital converter. As for the digital processing, after sampling the IF signal at 360 MHz, the range compression is obtained by multiplication by a replica signal, then the signal is re-sampled at 60 MHz. Then a FFT processing is applied to obtain amplitude and phase of the backscattered signal as a function of range. The last step is the real-time coherent integration of the complex samples over 1 ms. We choose to use the pulse pair processing technique [5], which provides amplitude and phase of the mean signal with an efficient noise reduction. The radiometric data (I&Q signals integrated on 1 ms) and the ancillary data (aircraft attitudes, GPS) are recorded at the same rate of 1 kHz. Fig.2 illustrates the block diagram of the digital processing of the received signal.

Absolute calibration was obtained from both internal (laboratory measurements) and external calibrations (using flights over 5 trihedral reflectors installed on a runway). Fig.3 shows the elevation antenna pattern obtained from the reflectors (symbols), the antenna pattern deduced from the anechoic chamber measurements (blue line) and the associated Gaussian fit (red dashed line). It may be seen that the shape and level of the antenna gain pattern retrieved from measurements over trihedral reflectors are remarkably consistent with the two-way gain pattern obtained from laboratory tests. Over the 3dB interval (≈7°-20°), the bias and rms difference between in-flight data and laboratory data are -0.2dB and ± 0.4dB, respectively.

For a typical sea surface backscatter in our conditions of measurement, the radiometric resolution is estimated to be ±0.2 dB for a signal post-integrated in time by pulse-pair integration over 30 ms.

Measurements over corner reflectors have also been used to assess the velocity estimates (not shown). Within the 3dB beamwidth the average bias and rms difference between measurements and expected velocity (accounting for aircraft velocity) are 0.4 m s^{-1} and 0.5 m s^{-1}, respectively.

Fig. 1. Geometry of observation, for both the LI and MI antennae

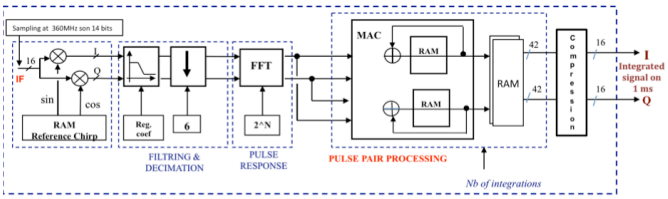

Fig. 2.Block diagram of the radar digital processing unit.

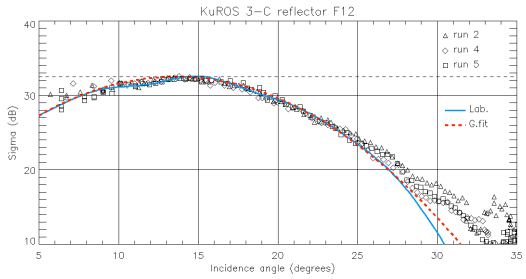

Fig. 3.Results of calibration flights over corner reflectors for the LI antenna. Each symbol (triangle, diamond, square) corresponds to one of the 3 successful overflights. For each overflight, only the reflector located the closest to the flight track (i. e., yielding the highest power backscatter signature) is displayed. Also shown are the antenna gain pattern obtained from the anechoic chamber measurements (blue line), and its Gaussian fit (red dashed line), with maxima coinciding with the 32.5 dBm^2 radar cross section of the trihedral reflectors at boresight.

III. Data Set, Processing Methods and Results

The first scientific data set of KuROS has been obtained during two campaigns held in 2013, namely the HyMeX campaign over the Gulf of Lion in the Mediterranean Sea [6] and the PROTEVS campaign near the coasts of Brittany (west of France). In 2013, KuROS has been successfully used for a total of 15 flights in different conditions of wind, waves, and current conditions (wind from 9 to 20 m/s,

waves from 1.4 to 6.1 m significant wave height, tidal currents during PROTEVS up to 2 m/s).

As explained above, the processing is focused in this work on the LI antenna data. Processing includes estimate of σ_0 as a function of incidence and azimuth, after gain and geometry compensation, as well as estimates of directional spectra.

A. Backscattering coefficient

Fig.4 shows two examples of the measured normalized radar cross-section σ° averaged over azimuth as a function of incidence angle. The case of flight #18 (respectively #04) corresponds to a wind speed of 9 m s^{-1} (respectively 14 m s^{-1}) and a significant wave height H_s of 5.3m (respectively 2.5 to 3 m). In Fig.4, the KuROS σ° profiles are compared to those predicted for the same wind, by the empirical Geophysical Model Functions (GMF) of [7] (plus signs). This model was built using a quasi-specular backscattering theory and a Gaussian surface assumption combined with observations of TRMM PR Ku band radar and is expected to be accurate for incidence angles $0 \le \theta \le 15°$. A quadratic multi-parameter fit to TRMM PR data sorted according to wind and significant wave height was also performed over the incidence angle range from 5° to 18°, from the large collocated data base compiled by [8]. The results are very close to the model [7]- not shown. Finally, Fig.4 also shows for comparison the GMF given by [9], based on the Ku band NSCAT scatterometer data. It may be seen that our measurements are very consistent with the TRMM model at low incidence angles, and in good agreement with NSCAT model although there is a trend of 0.5 to 1 dB overestimate of KUROS with respect to NSCAT model near 20° incidence.

Fig. 5 illustrates for the same case, the variation of σ_0 with azimuth for an incidence of 20°. This behavior shows an upwind to crosswind asymmetry of about 2B but for this wind speed, a non-significant upwind to downwind asymmetry. Results of Fig.4 and 5 show that although the LI antenna was not originally designed to estimate the wind vector, the data are appropriate to retrieve this parameter using an empirical model of the type of [9] applied for incidence angles close to 20°. Work is under progress for this retrieval. For future campaigns we will also use data at larger incidence (40°), which are more sensitive to wind variations.

B. Directional wave spectrum

For the estimation of directional wave spectrum the analysis of the modulations of radar reflectivity as a function of distance within the footprint permits to compute the directional sea wave spectrum along the direction of observation, while the rotation of the antenna around the vertical axis permits to explore all the azimuthal directions. The theory underlying this measurement technique was given by [3], and is briefly recalled here. The elementary backscatter cross-section σ is given by $\sigma = \sigma° A$, where A is the area contained within a radar range gate.

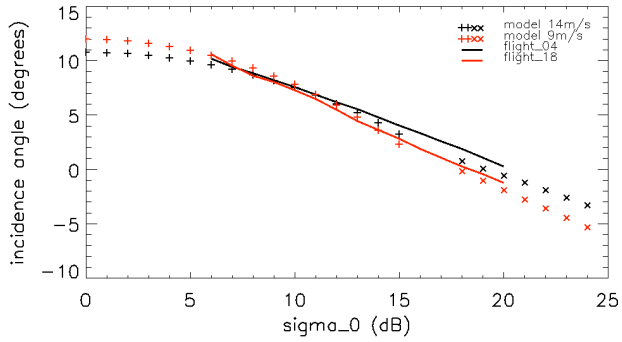

Fig. 4.Normalized radar cross section σ° averaged over the azimuthal directions (~120 s of data), as a function of incidence angle. Solid lines : Kuros data near the Lion buoy on 6 March 2013 (red line, flight 18, 12 : 28 UTC, wind speed 9 m s^{-1}) and on 6 february 2013 (black line, flight 04, 14:08 UTC, wind speed 14 m s^{-1}). Symbols: plus signs for the model of [7] derived from TRMM PR data; cross signs : empirical model of [9] derived from NSCAT data.

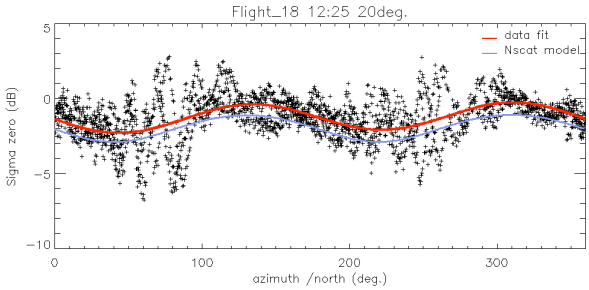

Fig. 5.Normalized radar cross-section at incidence 20° as a function of azimuth for the same conditions as the red line in Fig.4. Here the red line is a fit (Fourier developement with 2 harmonics), the blue line the NSCAT model [9] for the same wind conditions (9 ms^{-1}).

The fractional modulation m(x,φ) of the cross section seen by the radar is δσ/σ averaged laterally across the beam:

$$m(x,\varphi) = \frac{\int G^2(y)(\delta\sigma/\sigma)\,dy}{\int G^2(y)\,dy} \qquad (1)$$

where $G^2(y)$ is the two-way azimuth antenna gain pattern.
The sea wave polar-symmetric height spectrum F(k,φ) is then obtained from the expression (cf [3], [4]):

$$F(k,\varphi) = \frac{L_y}{\sqrt{2\pi}\ \cot\theta - \frac{\partial \ln\sigma_o}{\partial\theta}} \qquad (2)$$

where k, θ, and φ are wavenumber, incidence angle, and azimuth, respectively, L_y is a length related to the azimuthal width of the beam footprint, and $P_m(k,\varphi)$ is the modulation spectrum, defined as:

$$P_m(k,\varphi) = FT\left(m(x,\varphi)\right).\ FT^*\left(m(x,\varphi)\right) \qquad (3)$$

where *FT* refers to the Fourier transform operator, and * stands for complex conjugate.

As discussed in [3], the speckle noise of the radar technique produces an additional modulation of σ°, which is included in the measured modulation spectrum, and this speckle noise must then be removed from the data for precise quantitative studies. In order to estimate the spectrum of the speckle noise, [4] used a semi empirical method based on the comparison between data integrated over different time intervals. Another approach was proposed by [10] in the context of the processing of SAR images. These authors proposed to remove the speckle noise by computing image cross-spectra between pairs of single look SAR images separated in time. Following their approach, we replaced here the modulation spectrum $P_m(k,\varphi)$ of equation (3) by the quantity:

$$P'_m(k,\varphi) = \mathrm{Re}\,al\left\{FT\left(m(x,\varphi,t)\right).\ FT^*\left(m(x,\varphi,t+\delta t)\right)\right\} \qquad (4)$$

The time interval δt should be large enough that the speckle noises of both profiles are uncorrelated, but small enough that the radar resolution cell is only marginally displaced during that interval. Here we chose a time interval δt=66ms, which permitted both conditions to be well fulfilled. Nevertheless, due to imperfect correlation between the sea wave signals at times t and t+δt, the computed $P'_m(k,\varphi)$ happens to be negative on some scarce occurrences. Since the sea wave spectrum should be a positive definite quantity, those values are artificially set to zero. This has virtually no effect on the retrieved significant wave height. The results presented below have been obtained by using this cross-spectral approach and very similar to those obtained when the speckle is corrected by using the approach presented in [4].

The slope spectrum of the surface waves $k^2 F(k,\varphi)$ is then obtained using Eq. (2), and the mean trend of σ_0 with incidence estimated from the observations (over the range {8°-18°}). In order to remove the 180° ambiguity in the propagation direction, we used the cross-spectrum between σ_0 modulations (related to surface slopes) and surface velocity modulations (related to orbital modulations of the waves): for each spectral component, a positive (negative) correlation between these modulations denote waves going away from (approaching), the radar, so that the sign of the real part of this cross-spectrum gives the direction of propagation. Directional spectra of ocean waves contain information from different components related to different sources of generation (wind-waves generated locally, swell propagating from remote sites). Therefore it is essential to be able to distinguish different components in the 2D spectra. To do so, we have adapted a method based on a watershed partitioning algorithm [11] to take into account the noisy nature of the 2D spectra: while using the "watershed" method, we have applied noise reduction (averaging in wave number), discretization of energy levels, and an iterative scheme. In summary the processing of ocean wave spectra includes 4 steps:

- Fourier analysis of the radar cross-section modulations (using cross-spectrum analysis)
- Correction for the Tilt Modulation Transfer Function
- Ambiguity removal (using cross-correlations between σ_0 and velocity modulations)
- Partition of the wave spectra into up to 3 wave partitions (using an improved watershed algorithm)

Fig. 6 shows an example of the resulting directional spectrum. It is very consistent with the geophysical situation, as well as with buoy observations and model results: low energy wind waves propagating to North-West, in agreement with wind temporary from South-east and two more energetic swell components (peak wavelengths of 170 m and 180m), propagating to west-southwest (250° and 230°) in agreement with winds from East, North-East in the northern part of the basin.

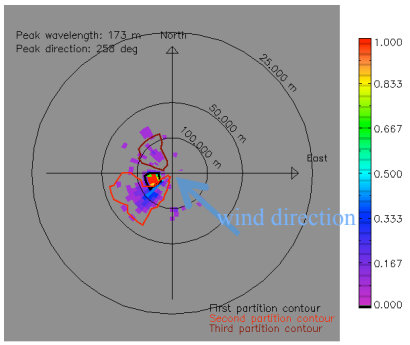

Fig. 6.Directional sea wave slope spectrum obtained from a 30 s sample of KuROS observations (case of March 6th 2013 12:26:31). The ambiguity in the propagation direction has been removed (see text). Energy density is in colour code, Concentric black circles indicate the wavelength. Direction is in the meteo-oceanic convention (North towards top of the figure, waves going to). Three partitions ar identified, sorted by decreasing energy (contours in black, red and brown). Wind at the time of measurement is 9 m s^{-1} from South-East.

After integration of wave energy over azimuths, the omni-directional wave spectra can be compared to non-directional wave rider observations. Fig. 7 illustrates the good consistency between omni-directional wave spectra obtained from KuROS with the buoy measurements.

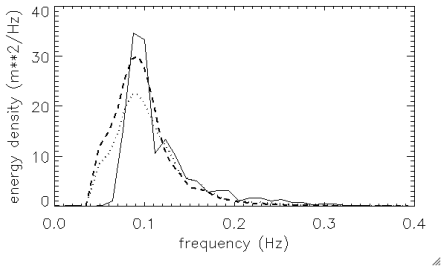

Fig. 7. Omnidirectional sea wave frequency spectrum as a function of wave frequency from the buoy (solid line) and from KuROS just before overflight of the buoy (dotted line), and just after overflight (dashed line).

C. Speckle analysis

Speckle is due to coherent backscatter from the surface small-scale facets whose size is smaller than the resolution (see e.g [12]). When the objective is to retrieve wave properties from radar ocean scenes, speckle may be a major issue. A possibility to minimize speckle is to use the method presented in Section III-B above. Nevertheless, for other applications or for different acquisition configurations (including CFOSAT), it remains important to understand and parameterize effect the speckle in order to be able to eliminate it from the signal modulation spectra. Over the ocean the coherence scales of the facets contributing to speckle (gravity-capillary waves) are notwell known and are probably highly variable with wind speed, direction of observation with respect to the wind direction, modulation by long waves and/or breaking waves. Signal coherence is also dependent of the geometry of observations: for an across-track elevation plane and a large azimuth footprint, the Doppler Bandwidth (~1 kHz for KuROS) is much larger than in the case of the along-track antenna pointing. This will decorrelate the signal much faster for across-track observations.

To study speckle properties, we have used two different methods. Method 1 is identical to the one presented in [4], and is based on the comparison between auto-spectra (Eq. 3) of the signal fluctuations estimated from data integrated over different time intervals (here we chose 33 ms and 99 ms). With method 2, the speckle energy density spectrum is derived from the difference between the auto-spectrum P_{auto} (Eq.3 for a 99 ms averaged signal) and the cross-spectrum P_{cross} (Eq.4 applied on two spectra of 99 ms time-integrated signals):

$$P_{sp} = \frac{(P_{auto} - P_{cross})}{1+\mu^2} \qquad (5)$$

where $1+\mu^2$ is a correcting term involving the total energy of the modulations (see [3]).

Fig. 8a-c show, for two 30s data sets of a same flight (wind speed ~14 m/s, fully-developed wind sea with significant wave height H_s~3 m), the speckle energy density spectrum averaged in azimuth. The difference between Fig. 8a and 8c is the aircraft route (see below). Fig.8a and 8c show that both methods give very similar results. Overall the energy of the speckle (integrated over wave numbers and azimuths) represents 26 to 37% (method 1) or 18 to 30% (method 2) of the energy of the wave spectra. The Gaussian model proposed by [3] to represent the speckle spectrum P_{sp} is:

$$P_{sp} = e^{-\frac{K^2}{2K_p^2}} \quad \text{with} \quad K_p = \frac{2\sqrt{\ln 2}}{\Delta X} \qquad (6)$$

where ΔX is related to the radar resolution projected on the surface, and N_{ind} is the number of non-correlated samples in the radar signal.

A fit of Eq.6 is plotted in Fig.8a-c. Although the Gaussian model is not completely satisfying at small wave numbers, it reproduces correctly the wavenumber dependence at k >0.08 rad m^{-1}. The fit provides the two parameters of the model (Eq. 6): K_p is about 0.21-0.22 (method 1) or 0.25-0.33 (method 2) i.e. ΔX between ~5 and 8m, in agreement with the horizontal resolution for incidence angles from 11 to 15°. N_{ind} spans between 114-136 (method 1) or 108-122 (method 2). This indicates that the mean correlation time of the signal is less than 1ms (0.7-0.9 ms). Note also that our preliminary analysis shows also that N_{ind} varies significantly with wind intensity and/or wave heights with N_{ind} increasing (speckle decreasing), when wind or wave height decreases. Fig. 8b and 8d show the azimuth behavior of the speckle density spectrum. It can be seen that the energy density spectrum of speckle exhibits a complex variation with azimuth: when the airplane flies parallel to the wind and wave direction (Fig.8b), there is a large variation of speckle with azimuth with a maximum along-track. In opposite, when the aircraft flies perpendicular to wind and waves (Fig. 8d), the speckle is almost isotropic. We explain these results by the fact that there is an additive (Fig.8b) or compensating effect §Fig. 8d) of speckle variations due to short waves anisotropy (speckle maximum along wind) and those due to the Doppler bandwidth variation with the antenna rotation (speckle maximum when antenna pointing along track). Work is in progress to assess this conclusion from the analysis of the whole data set.

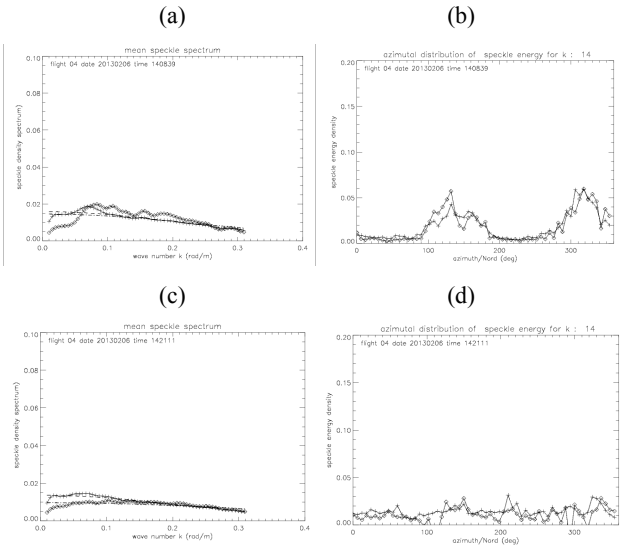

Fig. 8.Energy density of the speckle (in units of wave slope spectrum) for a 99 ms integrated sample. (a) and (c): mean value over all azimuth directions; (b) and (d) variation with azimuth at the peak of the wave spectrum (≈ 2π/90 rad/m) . (a-b) aircraft route is 140°, i.e almost parallel to the wind (120°) and wave propagation (130°). (c-d) same case but when aircraft route is 30°. + signs and diamonds: speckle estimated using method 1, respectively method 2.

IV. CONCLUSION

We have presented the main characteristics of the new airborne Doppler Ku-Band radar KuROS and the first results on ocean wave spectra. We find that the speckle-free wave directional spectra obtained by using the modulation transfer function according to [3] combined with profiles of σ° with incidence angles, are consistent with directional buoy observations, both in terms of significant wave height and principal parameters of the wavenumber spectrum (mean or

peak frequency and direction). The method based on the correlation between and discretization in energy gives consistent results for partitioning the 2D wave spectrum in different wave trains. A preliminary analysis of the speckle energy density spectrum indicates that the correlation time of the facets contributing to speckle is of the order of 1 ms but varies with surface conditions. It also indicates that variation of speckle with azimuth is complex and probably influenced by both variation of the Doppler bandwidth with the antenna rotation and by anisotropy of scatters on the surface.

ACKNOWLEDGMENTS

The authors wish to thank the staff of the LATMOS radar team for its involvement in the development or operations of Kuros. They also wish to thank the staff of the SAFIRE team who operated the ATR42 aircraft, and the Technical Division of CNRS-INSU for its support in the radar on-board implementation design. IETR (from CNRS, Rennes Université, INSA, Supélec) designed and built the antenna. The development and operation of the Kuros radar was funded by the French space agency CNES (Centre National d'Etudes Spatiales).

Parameter	**Value**
Frequency	13.5 GHz
Transmitted power	10 W
LI antenna	14° bore sight incidence angle; gain=18.5dB 18.5° elevation x 8.6° azimuth (one way), HH
MI antenna	40° bore sight incidence angle HH: 21° elevation x 8° azimuth beam width; gain=17.5dB VV: 17° elevation by 8° azimuth beam width; gain=18dB
SNR ratio (1 pulse)	LI antenna: 11.3dB ; MI antenna: -5.4dB
Antenna rotation	2.4 to 4.6 rotations /minute (tunable)
Aircraft speed	90 to 110 m/s

Table 1: Main parameters of the KuROS radar

REFERENCES

[1] Hauser D., C. Tison, J.-M. Lefevre, J. Lambin, T.Amiot, L. Aouf, F. Collard, and P. Castillan, Measuring ocean waves from space : Objectives and characteristics of the China-France Oceanography SATellite (CFOSAT), *Proceedings of the ASME 2010 29th International Conference on Ocean, Offshore and Arctic engineering, Volume 4,* Shanghai, China, june 6-11, 2010, pp. 85-90, doi : 10.1115/ OMAE2010-20184, 2010.

[2] Caudal G., D. Hauser, R. Valentin C. Le Gac, *Journal of Oceanic and Atmos. Tech*, in revision, 2014

[3] Jackson F. C., W. T. Walton, and P. L. Baker, Aircraft and satellite measurement of ocean wave directional spectra using scanning-beam microwave radars, *J. Geophys. Res., Vol. 90,* 987-1004, 1985.

[4] Hauser D., G. Caudal, G. J. Rijckenberg, D. Vidal-Madjar, G. Laurent, and P. Lancelin, RESSAC: A new airborne FM/CW radar ocean wave spectrometer, *IEEE Transactions on Geoscience and Remote Sensing, 30(5),* 981-995, 1992.

[5] Zrnic, D. S., Spectral moment estimates from correlated pulse pairs, *IEEE Trans. Aerosp. Electron. Syst.,* Vol. AES-13, 344-354, 1977.

[6] Drobinski P., V. Ducrocq, P. Alpert, E. Anagnostou, K. Béranger, M. Borga, I. Braud, A. Chanzy, S. Davolio, G. Delrieu, C. Estournel, N. Filali, Boubrahmi, J. Font, V. Grubisic, S. Gualdi, V. Homar, B. Ivancan-Picek, C. Kottmeier, V. Kotroni, K. Lagouvardos, P. Lionello, M. C. Llasat, W. Ludwig, C. Lutoff, A. Mariotti, E. Richard, R. Romero, R. Rotunno, O. Roussot, I. Ruin, S. Somot, I. Taupier-Letage, J. Tintore, R. Uijlenhoet, H. Wernli, HyMeX, a 10-year Multidisciplinary Program on the Mediterranean Water Cycle, *Bull. Amer. Meteorol. Soc., doi: http://dx.doi.org/10.1175/BAMS-D-12-00242.1,* 2013

[7] Freilich M. H., and B. A. Vanhoff, The relationship between winds, surface roughness, and radar backscatter at low incidence angles from TRMM Precipitation Radar measurements, *Journal of Atmospheric and Oceanic Technology, Vol. 20, 549-562, 2003.*

[8] Tran N., B. Chapron, and D. Vandemark, Effect of long waves on Ku-band ocean radar backscatter at low incidence angles using TRMM and altimeter data, *IEEE Geoscience and Remote Sensing Letters, Vol. 4, No. 4*, 542-546, 2007

[9] Wentz F. J., and D. K. Smith, A model function for the ocean-normalized radar cross section at 14 GHz derived from NSCAT observations, *J. Geophys. Res., 104, No. C5,* 11,499-11,514, 1999

[10] Engen, G., and H. Johnsen, SAR-Ocean wave inversion using image cross spectra, *IEEE Trans. Geosci. Rem. Sens., Vol. 33, No. 4,*1995.

[11] Hanson J.L. and O.M. Phillips, *J. Atmos. And Oceanic Tech. vol18, 2001, p 277-293*

[12] Ulaby, F. T., R. K. Moore, and A. K. Fung, 1982: Microwave Remote Sensing. Vol. II. Addison-Wesley, 1064 pp.

Table 2: Kuros parameters for the different modes of operation. H is the approximate flight level. PRI, Tp, Trep are respectively the Pulse Repetition Interval, the pulse duration and the replica duration. Frequency Band is that of the transmitted chirp. F_{repmax} is the maximum frequency of the replica. Analysis band $B_A=F_{repmax}-F_{emax}$ is the frequency band after deramping. N_{real} is the number of points after decimation. N_{FFT} is the number of points for FFT processing including zero padding. Signal to Noise Ratio (SNR) is given for one pulse.

Antenna	**H (m)**	**PRI (µs)**	**T_p (µs)**	**T_{rep} (µs)**	**Frequency Band (MHz)**	**Frepmax (MHz)**	**Analysis band (MHz)**	**N_{real}**	**N_{FFT}**	**S N R (dB)**
LI	3000	43.5	17	22.54	25-125	157.59	32.59	1352	2048	11.3
LI	2000	28.5	10.33	15.92	25-125	179.11	54.11	955	1024	16.6
LI	1000	16.5	5.66	8.56	25-125	176.24	51.24	514	512	25.6
LI	450	7.0	2	3.05	25-125	177.50	52.50	183	256	36.0
MI	3000	53.5	17	34.45	30-60	90.79	30.79	2067	2048	-5.4
MI	2000	37.0	10.33	24.48	30-60	101.09	41.09	1469	2048	-0.1
MI	1000	22.0	5.66	13.4	30-60	101.02	41.02	804	1024	8.9
MI	450	12.0	2	5.09	30-60	106.35	46.35	305	512	19.3